



1 **Autoregressive Statistical Modeling of a Peru Margin Multi-Proxy Holocene Record Shows**
2 **Correlation Not Causation, Flickering Regimes and Persistence**

3
4 **Seonmin Ahn¹, Baylor Fox-Kemper², Timothy Herbert², Charles Lawrence¹**

5
6 ¹Division of Applied Mathematics, Brown University

7 ²Dept. of Earth, Environmental, and Planetary Sciences, Brown University

8
9 *Correspondence Charles Lawrence

10 charles_lawrence@brown.edu

11 Division of Applied Mathematics.

12 Brown University

13 182 George Street

14 Providence, RI 02912

15
16 **Abstract**

17
18 Correlation does not necessarily imply a causation, but in climatology and paleoclimatology, correlation
19 is used to identify potential cause-and-effect relationships because linking mechanisms are difficult to
20 observe. Confounding by an often unknown outside variable that drives the sets of observables is one of
21 the major factors that lead to correlations that are not the result of causation. Here we show how
22 autoregressive (AR) models can be used to examine lead-lag relationships--helpful in assessing cause and
23 effect--of paleoclimate variables while addressing two other challenges that are often encountered in
24 paleoclimate data: unevenly spaced data; and switching between regimes at unknown times. Specifically,
25 we analyze multidimensional paleoclimate proxies, sea surface temperature (*SST*), C_{37} , $\delta^{15}N$, and %N
26 from the central Peru margin to find their correlations and changes in their variability over the Holocene
27 epoch. The four proxies are sampled at high-resolution but are not synchronously sampled at all possible
28 locations. The multidimensional records are treated as evenly spaced data with missing parts, and the
29 missing values are filled by the Kalman filter expected values. We employ hidden Markov models
30 (HMM) and autoregressive HMM (AR-HMM) to address the potential that the degree of variability and
31 the correlations between in these proxies appears to show changes over time. The HMM, which is not
32 autoregressive, shows instantaneous correlations between observables in two regimes. However, our
33 investigation of lead-lag relationships using the AR-HMM shows that the cross-correlations do not
34 indicate a causal link. Each of the four proxies has predictability on decadal timescales, but none of the
35 proxies is a good predictor of any other, so we hypothesize that a common unobserved variable--or a set
36 of variables--is driving the instantaneous relationships among these four proxies, revealing probable
37 confounding without prior knowledge of potential confounding variable(s). These findings suggest that
38 the variability at this site is remotely driven by processes such as those causing the Pacific Decadal
39 Oscillation, rather than locally driven by processes such as increased or decreased vertical mixing of
40 nutrients.

41
42 **Keywords:** Hidden Markov Model, Decadal Variability, Holocene, Pacific Decadal Oscillation,
43 Paleoclimate

44



45 1.0 Introduction

46 This paper examines statistical aspects of a long-duration, high-resolution, multi-dimensional time series
47 of four proxies (SST ; C_{37} ; $\delta^{15}N$; $\%N$) that record variations in marine conditions over the Holocene epoch
48 (0.60 to 9.44 kA B.P.). The sediment is sampled at high-resolution to amount to roughly 3-year averages
49 sampled every 7 years under the accumulation rate typical of the region. These records indicate both
50 surface and subsurface variability in the physical and biological state. It is expected that the evolving
51 relationships among these records over the Holocene reveal aspects of the mechanisms responsible for
52 variabilities, such as correlations, timescales, and predictability.

53

54 The four records examined are proxies for sea surface temperature (SST) through the alkenone proxy,
55 biological productivity of a specific phytoplankton group (C_{37}) through analyses of the abundance of
56 alkenones (representing haptophyte algal productivity), subsurface properties through analyses of $\delta^{15}N$, an
57 index of subsurface oxygenation and denitrification, and the percentage of organic nitrogen ($\%N$) which
58 is a composite of all biological inputs to the sediment. Interannual and decadal variability is observed in
59 subsurface oxygen fluxes and concentrations worldwide, but particularly in the eastern tropical South
60 Pacific oxygen minimum zone where this core is located (Bopp et al. 2002, Stramma et al. 2008). These
61 studies suggest that a combined examination of 1) warming of the ocean surface (here recorded through
62 alkenone SST), 2) changes in stratification (here recorded through upwelling as indicated via productivity
63 C_{37} and $\%N$), 3) changes in ecological makeup (here recorded through a comparison between $\%N$ which
64 indicates a combined productivity of all organisms and C_{37} which indicates productivity of only some
65 organisms), and 4) changes in the oxygen utilization at depth (here proxied through $\delta^{15}N$) may help
66 explain the combination of thermal, dynamical, and biogeochemical factors contributing to the variability
67 in this region. Sediment samples were placed on an age scale based on a polynomial fit to 8 radiocarbon
68 dates - the resulting age model has an uncertainty on the order of 100 yr.

69

70 Some of the key questions in this region are whether the variability is from a local or internal source, such
71 as variation in physics through mixing or eddies at the surface (Brink et al., 1983, Colas et al. 2012) or
72 changes in the biological makeup of ecosystems in the region (e.g., Gooday et al. 2010), or from a remote
73 or external source, such as variations in the water properties arriving at the site through large scale modes
74 such as El Nino or the Pacific Decadal Oscillation (Mantua et al. 1997, Deser et al. 2010). The site (Fig.
75 1) is known for wind-driven upwelling (Brink et al. 1983) at depths shallower than 250m and low oxygen
76 concentrations at depth typical of the eastern tropical South Atlantic oxygen minimum zone, which has
77 been highly variable near 250m depth in recent times (Stramma et al. 2008). Despite the low oxygen
78 levels at depth, the typical sediment accumulation rate over the Holocene during these samples is high (70
79 cm/kyr), which suggests high, sustained biological productivity and presumably a persistent level of
80 oxygen demand.

81

82 A visual analysis of the proxy records (Fig. 2) suggests that the variability of four proxies might fall into
83 multiple regimes: one state with high variability and another state with low variability. This *biphasic*
84 behavior guided our initial analysis using a Hidden Markov Model (HMM; Rabiner, 1989). Hidden
85 Markov methods are increasingly used in identifying climate regime shifts (e.g., Majda et al. 2006,
86 Franzke & Woollings 2011, Ahn et al. 2017).

87



88 A less common tool in climate modeling is the autoregressive hidden Markov method (AR-HMM,
89 Hamilton, 1988, 1989, 1994) which allows for some memory in the system through a dependence on
90 previous proxy values as well as correlations in the present proxy value noise. Both our HMM and AR-
91 HMM results show that there exist two regimes of variability in proxy space at site MW8708-PC2. Here
92 the AR-HMM technique will be used to probe deeper into distinctions between causality and correlation,
93 under the premise that a predictive cause should precede its effect in time. A surprising result of this study
94 is that our conception of the relationships among these proxies changed dramatically when this technique
95 was applied and contrasted to the more standard HMM approach. The AR-HMM shows that both regimes
96 show high auto-correlation and low cross-correlation, thereby indicating that none of the proxies are good
97 predictors of other proxies on interannual timescales. In cases in which regime change is not present, a
98 simpler autoregressive only model will be sufficient to assess predictive cause. The software provided
99 with this paper (<https://github.com/seonminahn/ARHMM>) can be applied for the analysis of multi proxy
100 data from a core record. When inferences on predictive cause between cores is of interest, it is essential to
101 account for uncertainty in age estimates to ascertain the significance to a putative lead/lag
102

103 **1.1 Context from Modern Observations**

104 To better understand what processes would affect the variability on the timescales that are sampled, a
105 brief analysis of the region and related climate indices was carried out. The location is somewhat south of
106 the region most active during the El Niño/Southern Oscillation (ENSO) cycles (i.e., south of NINO1,
107 Rasmusen & Carpenter, 1982). On longer timescales, a meridionally broader, yet similarly shaped
108 pattern of variability has come to be known as the Pacific Decadal Oscillation (PDO) (Deser et al. 2010).
109

110 Fig. 1(a) shows the location of the MW8708-PC2 sediment core that is analyzed for this study. The
111 location is superimposed on a map of the correlation of global sea surface temperature with the nearest
112 HadISST data point (15.5S, 75.5W). Warming in this region correlates well with warming along the
113 central and eastern equatorial Pacific, cooling over most of the extratropical Pacific, and weakly
114 correlates with temperatures in other basins. The correlated pattern resembles both the El Niño pattern
115 and the Pacific Decadal Oscillation pattern (Deser et al. 2010). In time, the sediment record (indicated by
116 circles in Fig.1b) is too infrequent to capture El Niño variability, generally taken to dominate the 2-7 year
117 band. While some of the biggest El Niño events (1982-3, 1997-8) are still visible in the filtered data, it is
118 evident that time filtering similar to our sediment sampling has removed most of the high-frequency
119 ENSO variability.
120

121 Deser et al. (2010) follow Mantua et al. (1997) in tracking the Pacific Decadal Oscillation using the first
122 empirical orthogonal function (EOF) and principal component (PC) of North Pacific sea surface
123 temperature (20N to 70N, 100E to 100W) after the removal of seasonal and global mean variability. Its
124 variability is taken as a PDO index. This index captures much of the low frequency (>7yr) variability near
125 the sediment location (Fig. 1b), even though the core location is remote from all data included in the PDO
126 index and the monthly index and core location SST have a correlation coefficient of only 0.16. Running
127 means over 2 to 22-years of SST at our site correlates with the PDO index all have correlation coefficients
128 above 0.53, and the peak coefficient is just above 0.6 (for 7-year averages). Thus, we interpret the
129 dominant mode of variability accurately sampled by the core measurements to be associated the Pacific
130 Decadal Oscillation. Note that the record described here is significantly longer than extant records of the
131 PDO (e.g., AD 993-1996 tree-ring compilation by McDonald & Case, 2005).



132
133 A variety of mechanisms have been used to explain the PDO. Alexander (2010) reviews the mechanisms
134 and concludes that a variety of causes are consistent with the observations, mainly heat flux and wind
135 variability, including El Nino variability communicated to the N. Pacific by the “atmospheric bridge”.
136 This variability is modulated toward lower frequencies by the reddening of “stochastic” variability
137 (Hasselmann, 1976) by the large heat capacity of the mixed layer (Frankignoul & Hasselmann, 1977), but
138 also through slow-response phenomena such as the re-emergence of sub-boundary-layer temperature
139 anomalies during subsequent winters and the slow propagation of baroclinic Rossby waves. The
140 autoregressive formulation of the AR-HMM is essentially the same as the stochastic model used by
141 Hasselmann. According to Frankignoul & Hasselmann (1977), forcing amplitude affects response
142 amplitude, but the damping rate of variability affects both the magnitude of variability and the persistence
143 timescale, with greater magnitude and longer persistence indicating weaker damping which is a
144 consequence of a shallower mixed layer and reduced heat capacity.

145 146 **2.0 Method**

147 **2.1 Data Collection**

148 High-resolution records of four paleoclimate indicators are collectively analyzed for a sediment core
149 retrieved from the central Peru margin (Site MW8708-PC2: 15.1°S, 75.7°W, water depth of 250m, Fig.
150 1). This site has an extremely high and steady sedimentation rate (70cm/kyr) across most of the Holocene
151 (10kA - 1.4 kA), and frequently contains annual laminations. Records are obtained from 2cm (3 years)
152 slices taken every 5cm (7 years). The age model determined the core top to be located at ~600 years
153 before present (bp), (gravity coring typically disturbs the upper few decimeters of sedimentation and the
154 base of the record to lie at ~9440 yr bp. The very gentle curvature in estimated sediment accumulation
155 rates (Chazen et al., 2009) will be ignored in this study, so depth is proportional to age and time steps are
156 uniform.

157 158 **2.2 Missing Data**

159 The four proxies are measured in high-resolution with fairly uniform depth sampling (2cm about every
160 5cm), but different proxies are not sampled at all possible locations. In order to compose an evenly-
161 spaced data set that will be used to train discrete-time statistical models described below, the expected
162 values in an evenly-spaced record are used to fill in the records using a Kalman filter (Little & Rubin,
163 1986; Viefers, 2011). The Kalman filter finds the expected value of the missing data given the observed
164 value, and we find the maximum likelihood estimates of the model parameters by using the expectation-
165 maximization algorithm. Before doing so, time from 0 to 563 discrete time steps (each of which
166 represents 5cm/7yr) is discretized into 1127 discrete half-time-steps (each of which represents
167 2.5cm/3.5yr, or approximately the width of an analysis slice). Each proxy analysis is then allocated to the
168 half-time-step nearest its location in depth/age. Not every possible slice was analyzed: there are 526 SST;
169 526 C_{37} ; 727 $\delta^{15}N$; and 728 %N measurements out of 1127 possible to fill all half-time-steps.

170
171 Each half-time-step is interpreted as a 4-component vector of observations $X(t)$.

$$172 \quad X(t) = \begin{bmatrix} x_1(t) \\ x_2(t) \\ x_3(t) \\ x_4(t) \end{bmatrix} = \begin{bmatrix} (SST(t) - \langle SST \rangle) / \sigma_{SST} \\ (C_{37}(t) - \langle C_{37} \rangle) / \sigma_{C_{37}} \\ (\delta^{15}N(t) - \langle \delta^{15}N \rangle) / \sigma_{\delta^{15}N} \\ (\%N(t) - \langle \%N \rangle) / \sigma_{\%N} \end{bmatrix}$$



173 In the climate and data assimilation literature, this vector is usually called the “state” vector; here it will
 174 be called the observation vector to distinguish it from the regime or “state” of the hidden Markov model.
 175 After arranging the data in this manner, the expected values estimated using a Kalman filter are used to
 176 fill in missing data (Figs. 3, 4). The mean and standard deviation of each proxy variable have been
 177 removed as a preprocessing step so that the different units of each measurement are not a factor and the
 178 Kalman filter likewise does not depend on the units of measurement. Our preparation of this discrete-time
 179 technique and the discrete-time statistical models below assume that even spacing in depth is sufficiently
 180 uniform in time, i.e., variations in the age-depth relationship were not considered in this imputing
 181 technique.

182

183 2.3 Statistical Models: HMM and AR-HMM

184 The degree of variability in correlation among these proxies appeared to change at unknown times over
 185 this epoch. Visual analysis suggests that the correlations and variability of the four proxies varied over
 186 time in a potentially abrupt manner (Figs. 2, 3, 4). Indeed, use of a two-state (a.k.a. two-regime) hidden
 187 Markov models (HMM) and a generalization of this approach, autoregressive HMM (AR-HMM), do
 188 detect two distinct states at this site, characterized by different levels of variability and predictability.
 189 Experimentation with higher numbers of states revealed that two states were sufficient for this record.

190

191 Two-state hidden Markov models are considered using two different emission (time-correlation or
 192 memory) models. The first model assumes conditional independence among observations given the state,
 193 regime, and the second model considers direct dependence with adjacent observations (i.e., memory). The
 194 first one is consistent with a general vector, or multivariate Hidden Markov Model (HMM), and the
 195 second one is called the autoregressive hidden Markov model (AR-HMM), which is also known as a
 196 switching autoregressive model (Hamilton, 1988, 1989, 1994). Both models have hidden regimes or
 197 “states” in which it is assumed that the historical dependence of the current hidden (unobserved) state is
 198 entirely accounted by the state of its immediate preceding neighbor and a transition probability, i.e., the
 199 state-switching process is Markovian. The matrix of state transition probabilities is

200

$$a_{ij} = P(s(t+1) = j | s(t) = i)$$

201

The difference between the AR-HMM and HMM models is the relationship between the observations at
 202 different times. The equation for the AR-HMM can be written

203

$$X(t) = c_{s(t)} + \theta_{s(t)} X(t - \Delta t) + \epsilon(t)$$

$$\begin{bmatrix} X_1(t) \\ X_2(t) \\ X_3(t) \\ X_4(t) \end{bmatrix} = \begin{bmatrix} c_1 \\ c_2 \\ c_3 \\ c_4 \end{bmatrix} + \begin{bmatrix} \theta_{11} & \theta_{12} & \theta_{13} & \theta_{14} \\ \theta_{21} & \theta_{22} & \theta_{23} & \theta_{24} \\ \theta_{31} & \theta_{32} & \theta_{33} & \theta_{34} \\ \theta_{41} & \theta_{42} & \theta_{43} & \theta_{44} \end{bmatrix} \begin{bmatrix} X_1(t - \Delta t) \\ X_2(t - \Delta t) \\ X_3(t - \Delta t) \\ X_4(t - \Delta t) \end{bmatrix} + \begin{bmatrix} \epsilon_1(t) \\ \epsilon_2(t) \\ \epsilon_3(t) \\ \epsilon_4(t) \end{bmatrix} \quad (1)$$

204

There are two constant vectors $c_{s(t)}$, which are selected depending on the state at time t . Likewise, the
 205 autocovariance regression matrix ($\theta_{s(t)}$) that prescribes the deterministic part of the model evolution
 206 based on observations at a previous time and the noise covariance matrix ($\Sigma_{s(t)}$) that prescribes the
 207 stochastic part of the model evolution also have two versions which are selected based on state. The noise
 208 vector ($\epsilon(t)$) is chosen at each time from a Gaussian white noise distribution with zero mean and
 209 covariance matrices $\Sigma_{s(t)}$ that contain all of the information about stochastic variances and covariance of
 210 the observations.

211



212 The HMM can be written the same way as (1), but removing the deterministic dependence of current
213 observations on previous observations ($\theta = 0$). The HMM assumes that each observation follows
214 multivariate normal distribution with means (c), (stochastic) variances (Σ_{ii}), and (stochastic) covariances
215 (Σ_{ij}) determined only by present value of the hidden state.

216

217 In both the HMM and AR-HMM models, the unknown parameters including constant parameters in each
218 two-state model are estimated by the Baum-Welch expectation maximization algorithm (EM; Rabiner,
219 1989).

220

221 3.0 Parameter Estimation Results

222 The parameter estimations are done using the EM algorithm for both HMM and AR-HMM. The EM
223 algorithm updates parameters iteratively using the forward and backward sampling algorithm. The data
224 augmentation step that uses the Kalman filter is added at the beginning of each iteration to address
225 missing data. Depending on initial conditions of the EM algorithm, it is possible that the EM algorithm
226 converges to local maximum estimators instead of global maximum estimators. To avoid local maxima,
227 parameter estimations are repeated with 100 different initial conditions and the selected parameters are
228 those that achieve maximum likelihood from this set.

229

230 3.1 HMM Parameters

231 For a two-state HMM after removal of the overall mean and normalization of the standard deviation of
232 each proxy, there are five unknown parameters which have 32 degrees of freedom in total: the transition
233 matrix a , and one version of c and Σ for each state. Table 1 shows the results of the parameter
234 estimations. The two states are distinctively different in means and covariance. The mean of each proxy
235 differs in sign between the two states, which must be the case as the overall mean of each proxy has been
236 removed. However, the pattern of means among the proxies, e.g., high SST and low C_{37} , is a signature of
237 each state. The absolute values of the components and eigenvalues of Σ are larger in state 1 than in state
238 2. The eigenvalues (the strength of correlated noise components) of Σ are 2.21, 0.98, 0.57, and 0.18 for
239 state 1 and 0.82, 0.58, 0.20, and 0.13 for state 2. Thus, we can associate state 1 as a “noisy” state and state
240 2 as a “calm” state, because the proxies tend to fluctuate more when in state 1 than in state 2. In terms of
241 transition probability, the diagonal elements of a are close to 1, which implies that there is a high
242 probability of staying in a state. Table 2 shows that 7 of the 12 correlation coefficients are approximately
243 0.5 or higher.

244

245 According to the parameter estimations, the most probable state is determined at each time using the
246 backward sampling (Fig. 3). The median (mean) time to remain in HMM state 1 over 1000 samples is 70
247 years (128.6 years). The median time to remain in state 2 over 1000 samples is 91 years (189.8 years).

248

249 3.2 AR-HMM Parameters

250 For a two-state AR-HMM after removal of the overall mean and normalization of the standard deviation
251 of each proxy, there are seven unknown parameters which have 64 degrees of freedom in total: the
252 transition matrix a , and one version of c , θ , and Σ for each state. The estimated parameters are shown in
253 Table 2, and the model state and imputed values are shown in Fig. 4. Again, state 1 can be identified as
254 the “noisy” state and state 2 is “calm”. In terms of transition probability, the diagonal components of a are
255 around 0.8, which are smaller than those of the HMM. Thus, there are more frequent state changes in Fig.



256 4 than shown by the HMM (Fig. 3). The median (mean) time to remain in state 1 over 1000 samples is 7
257 years (17.9 years). The median time to remain in state 2 over 1000 samples is 28 years (39.8 years).

258

259 The diagonal entries of θ are close to 1 on both states: each variable of state 2 depends strongly on its
260 own past value. The diagonal entries of θ for state 1 are smaller than that of state 2 with both greater than
261 0.85 for all four proxies. The off-diagonal entries are all smaller than 0.07 for both matrices. Thus, only a
262 small part of the dependence of each variable on its past value can be attributed to cross-correlations
263 rather than autocorrelations. The antisymmetric components of θ are much smaller than the diagonal
264 components, so the “probability angular momentum” which lends covariant predictability (Weiss et al.
265 2016, Zia et al. 2016) is not significant.

266

267 The diagonal entries of Σ in the AR-HMM are much smaller than they were in the HMM--so that
268 variability attributed to noise within each variable is considerably lessened by the introduction of
269 memory. The eigenvalues of the Σ matrix as well are roughly a factor of 5 to 50 smaller, indicating that
270 the covariant modes of noise are estimated to be much weaker when the memory of the AR-HMM system
271 is permitted.

272

273 The mean state c of the HMM and AR-HMM do not resemble one another in its pattern, magnitude or
274 sign. Thus, while these patterns are a characteristic of the HMM and AR-HMM states, there is no
275 agreement between the pairs of states in mean, timing of onset, or cross-correlations.

276

277 3.3 Comparison of Models

278 The HMM is a special case of the AR-HMM. As the HMM may be formed from the AR-HMM, the fact
279 that the AR-HMM does not resemble the HMM implies that the lagged time information is a critical
280 aspect of the data. Thus, a key conclusion from the statistical models is that the lagged autocorrelations
281 are significantly better predictors of proxy variability than the different proxy-to-proxy cross-correlation
282 either at lagged times or as induced by correlated noise (Fig. 5). This fact implies that the different
283 proxies are not causally related to one another, as is often assumed in multi-proxy paleoclimate analyses
284 (Hu et al. 2017). Thus, in this location, the four proxies (SST ; C_{37} ; $\delta^{15}N$; $\%N$) are not related to each other
285 in the local sense that variability in any one dominates or contributes significantly to variability in another
286 through a local physical or biological mechanism.

287

288 For reference, the mean and variance of each proxy are given for noisy state (state 1) and calm state (state
289 2) of the HMM and AR-HMM in Tables 1 and 5. While both AR-HMM and HMM attribute a noisy state
290 and a calm state to the time series, none of the means, variances, or timing of onset of these states agree.
291 Furthermore, it was noted that the HMM mean states must be opposite in sign in order for the normalized
292 time series to be zero. The AR-HMM is not constrained by this limit, as the predictions of θ can contribute
293 to the mean. Because the AR-HMM is more general than the HMM, disagreement between these state
294 identifications indicates that the autoregression memory of the AR-HMM is important. Bolstering this
295 idea is the fact that the dominant modes of correlation of observations with the previous time observations
296 are autocorrelations, i.e., the dominant predictor of any of the four proxies is itself at a previous time and
297 not interactions between the observed variables.

298



299 For the comparison with the AR-HMM, the correlations of the four proxies in HMM are estimated as in
300 Tables 3-4. These correlation matrices are calculated using each data set in which the missing parts have
301 been imputed by their expected value and the state estimation at each time. The signs of correlations are
302 usually the same between the two model assessments, but the strength of the cross-correlations vary
303 somewhat. Note that the cross-correlations do not disappear in the AR-HMM. Even though the full model
304 reveals the underlying autocorrelations, these simple single-time correlations are unable to detect any
305 inconsistencies that correlations between variables do not reveal causation between variables in this data.
306

307 **4.0 Discussion**

308 The preceding statistical model results may be related back to the original science questions that
309 motivated this collection of data. That is, what changes in physics or biological makeup helps better
310 understand the mechanisms at play in setting the variability in this region?
311

312 **4.1 Implications for Mechanisms**

313 In the introduction, it was argued that potential local mechanisms might be used as causes to explain
314 correlations and connections among these data. Variability in upwelling, stratification, biological makeup,
315 oxygen utilization and productivity, and many other mechanisms would be likely to strengthen a
316 particular set of cross-correlations and levels of variability among these data. Indeed, two different states,
317 one noisy and calm, were detected with both AR-HMM and HMM model parameter estimation. Tables 1,
318 3, 4, and 5 show significant cross-correlations and difference in cross-correlations and levels of variability
319 between these two states. The typical HMM approach confirmed roughly these conclusions.
320

321 However, a closer examination of the dependences of the proxies on AR-HMM autocorrelations with
322 their previous time values and cross-correlations with previous and synchronous values of other proxies
323 reveals a very different story. This analysis revealed that the restrictions required to reduce the AR-HMM
324 to the HMM, i.e., the neglect of memory of past observations, systematically corrupted interpretation of
325 the system. The magnitude of the components and eigenvalues of the Σ matrix are significantly smaller in
326 the AR-HMM than in the HMM. Thus, present observations are caused--in the Granger (1969) sense--by
327 the previous observations, i.e. the predictive rather than the intervention sense. The small off-diagonal
328 terms in θ indicate that each proxy is not strongly caused by any other proxy, only by its own previous
329 values. Rather, the apparent correlations found by the HMM model very likely stem from confounding
330 (<https://explorable.com/confounding-variables>) by an unobserved mechanism that drives all four
331 parameters in a coordinated manner. These results are inconsistent with any local mechanism that would
332 link these proxies to one another causally, e.g., if *SST* variability were to indicate upwelling that drives
333 productivity and thus C_{37} and $\%N$. Because both the past-time cross-correlations and the present-time
334 correlated noise became less consistent in the AR-HMM when compared to the HMM, it is unlikely that
335 this lack of cross-predictability is due to the limited temporal resolution. Consistent local mechanisms
336 would require variability caused by unobserved mechanisms that might affect one or more of the proxies,
337 so-called confounding variables. A variety of distinct remote causes for variability, e.g., *SST* driven by the
338 PDO and other proxies driven by other climate modes or source variability, are a sufficient explanation
339 for the results here.
340

341 **4.2 Implications for Predictability**



342 One interesting aspect of the AR-HMM model is that it reveals the dependence of the present
343 observations on previous observations. This implies a sort of predictability of the four proxies based on
344 the AR-HMM. However, because the predictability is essentially just autocorrelations, the AR-HMM
345 does not predict significantly differently from persistence (same observations next time as this time).
346 Nonetheless, some aspects of predictability in this system are of interest.

347
348 One difference between a prediction system and a reanalysis of past events is that a prediction system
349 should use only the data that precedes the times that will be predicted. Two methods to achieve this were
350 used here: 1) predict new parameters using the data sequence preceding the points we predict, and 2)
351 sample values using these parameters.

352
353 Predictability of the AR-HMM was evaluated over two time windows: 236-266 and 535-563 cm depth.
354 Fig. 6 gives a sense of what behaviors these predictions tend toward in the 236-266 window. The interval
355 236-266 is chosen because the resolution of the interval 236-266 is relatively higher than other intervals,
356 and the AR-HMM state is persistently in the (calm) state 2 over this interval. Taking 266 as an endpoint,
357 the predictability of one-step to thirty-step is assessed. The interval 535-563 includes the most recent data
358 and tends to remain in the (noisy) state 1. Each prediction is repeated 1000 times.

359
360 Depending on the most probable state of an initial point, the entries of the next step are computed with the
361 emission model (equation (2)) with parameters estimated in the previous section. The state of the next
362 step is determined by the transition probability, and then the entries of the following step are computed
363 with the equation (2) in the same way. State determination and entry computations are repeated until
364 reaching the endpoint.

365
366 The accuracy of predictability based on the AR-HMM is examined using mean squared errors (MSE).
367 Predictions up to four-step, which corresponds to approximately three decades, achieve reduction of the
368 MSE by 40-80%, depending on the proxy. The results do not show a tight range of prediction when the
369 length of prediction is longer than four steps ahead. However, the probability of remaining in a given state
370 or regime for the future steps can be predicted from the transition probability, typically for decades based
371 on the AR-HMM transition probabilities. The noisiest proxies tend to have forecasts that revert to
372 spanning their climatological range most quickly. The forecasts that begin in the noisy regime of state 1
373 tend to lose persistence faster as well.

374
375 In order to compare the HMM with the AR-HMM, we assessed the predictability of the HMM is assessed
376 in the same manner as the that of AR-HMM. While the MSEs increase as the forecast length increases in
377 AR-HMM predictions, the MSEs of HMM keep the same size regardless of prediction length. In a system
378 with strong auto-correlations such as this one, useful forecasts require a memory of past states.

379 5.0 Conclusions

381 Multi-proxy records are a potentially powerful tool in strengthening understanding of paleorecords.
382 However, depending on which variables are observed and where, they may or may not capture direct
383 evidence of the mechanisms at work. This study was carefully designed to distinguish different types of
384 local mechanisms that might be causing variability on the Peru margin over the Holocene. However, it is



385 our interpretation of the estimates of statistical model parameters found that no local causal mechanisms
386 were observed to be significant at the roughly decadal scale of sampling employed.

387
388 This study illustrates the importance of assessing predictive (Granger) causation in order to avoid
389 spurious diagnoses of the mechanism through the use of autoregressive (AR) models for example. AR
390 algorithms are widely available (in R and MATLAB) for cases not involving regime change. In addition
391 as pointed out by Hu et al. (2017), when multiple records are involved, age uncertainty can also lead to
392 spurious associations.

393
394 Before closing, it is interesting to consider broadly the implications of the regime-switching observed
395 here. While it was shown that similar-sampling-frequency analyses of modern observations at this
396 location reveal SST variability that is dominated by the PDO, past variability indicates a change in PDO
397 variability at this site, transient appearance of other dominant modes, or changes in teleconnections.
398 Stevenson et al. (2012) demonstrate that changes in such remote influences of climate variability are
399 likely to be common even when the underlying climate mode is unchanging.

400
401

402 **Funding**

403 BFK was supported by NSF 1245944.

404

405 **Author Contributions**

406 Conceptualization, T.W. and C.E.L; Methodology, S.A. and C.E.L; Software, S.A.; Formal Analysis,
407 S.A., B.F.-K., T.W., and C.E.L; Data Curation, T.H; Writing, S.A., B.F.-K., T.W., and C.E.L;
408 Visualization S.A.

409

410 **Acknowledgements**

411 Conversations with Steve Clemens, Warren Prell, Jim Russell, Jeff Weiss, and Deborah Khider greatly
412 improved this work.

413

414 **References**

- 415 Ahn, S., Khider, D., Lisiecki, L., & Lawrence, C. E. (2017). A probabilistic Pliocene-Pleistocene stack of
416 benthic $\delta^{18}\text{O}$ using a profile hidden Markov model. *Dynamics and Statistics of the Climate System*.
417 Brink, K. H., D. Halpern, A. Huyer, and R. L. Smith (1983), The physical-environment of the Peruvian
418 upwelling system, *Prog. Oceanogr.*, 12(3), 285–305, doi:10.1016/0079-6611(83)90011-3.
419 Chazen, C. R., et al. (2009). Abrupt mid-Holocene onset of centennial-scale climate variability on the
420 Peru-Chile Margin, *Geophysical Research Letters* 36(18)
421 C. Deser, A. S. Phillips, and M. A. Alexander, “Twentieth century tropical sea surface temperature trends
422 revisited,” *Geophys. Res. Lett.*, vol. 37, no. 10, p. L10701, 2010.
423 Frankignoul, C. and Hasselmann, K., 1977. Stochastic climate models, Part II Application to sea-surface
424 temperature anomalies and thermocline variability. *Tellus*, 29(4), pp.289-305.
425 C.L.E. Franzke and T. Woollings, 2011: On the persistence and predictability properties of North Atlantic
426 climate variability. *J. Climate*, 24, 466–472.



- 427 Hu, J., Emile-Geay, J. and Partin, J., 2017. Correlation-based interpretations of paleoclimate data—where
428 statistics meet past climates. *Earth and Planetary Science Letters*, 459, pp. 362-371.
- 429 Gooday AJ, Bett BJ, Escobar E, Ingole B, Levin LA, Neira C, Raman AV, Sellanes J. Habitat
430 heterogeneity and its influence on benthic biodiversity in oxygen minimum zones. *Marine Ecology*.
431 2010 Mar 1;31(1):125-47.
- 432 Granger, C.W., 1969. Investigating causal relations by econometric models and cross-spectral methods.
433 *Econometrica: Journal of the Econometric Society*, pp.424-438.
- 434 J. D. Hamilton, “Rational-expectations econometric analysis of changes in regime,” *Journal of Economic*
435 *Dynamics and Control*, vol. 12, no. 2, pp. 385–423, 1988.
- 436 J. D. Hamilton, “A New Approach to the Economic Analysis of Nonstationary Time Series and the
437 Business Cycle,” *Econometrica*, vol. 57, no. 2, pp. 357–384, Mar. 1989.
- 438 J. D. Hamilton, *The Time Series Analysis*. Princeton University Press, 1994.
- 439 Hasselmann, K., 1976. Stochastic climate models part I. Theory. *Tellus*, 28(6), pp. 473-485.
- 440 B. Huang, V. F. Banzon, E. Freeman, J. Lawrimore, W. Liu, T. C. Peterson, T. M. Smith, P. W. Thorne,
441 S. D. Woodruff, and H.-M. Zhang, “Extended Reconstructed Sea Surface Temperature Version 4
442 (ERSST.v4). Part I: Upgrades and Intercomparisons,” *Journal of Climate*, vol. 28, no. 3, pp. 911–930,
443 2015.
- 444 J. J. Kennedy, N. A. Rayner, R. O. Smith, D. E. Parker, and M. Saunby, “Reassessing biases and other
445 uncertainties in sea surface temperature observations measured in situ since 1850: 1. Measurement
446 and sampling uncertainties,” *Journal of Geophysical Research: Atmospheres*, vol. 116, no. 14, p.
447 D14103, 2011.
- 448 Lax M, 1960. *Reviews of modern physics* 32, 25.
- 449 R. J. A. Little and D. B. Rubin, *Statistical analysis with missing data*. John Wiley & Sons, Inc., 1986.
- 450 A.J. Majda, C. Franzke, A. Fischer, and D. Crommelin, 2006: Distinct metastable atmospheric regimes
451 despite nearly Gaussian statistics: A paradigm model. *Proc. Natl. Acad. Sci. USA*, 103, 8309–8314.
- 452 N. J. Mantua, S. R. Hare, Y. Zhang, J. M. Wallace, and R. C. Francis, “A Pacific Interdecadal Climate
453 Oscillation with Impacts on Salmon Production,” *Bull. Amer. Meteor. Soc.*, vol. 78, no. 6, pp. 1069–
454 1079, Jun. 1997.
- 455 MacDonald, G.M. and Case, R.A., 2005. Variations in the Pacific Decadal Oscillation over the past
456 millennium. *Geophysical Research Letters*, 32(8), [dx.doi.org/10.1029/2005GL022478](https://doi.org/10.1029/2005GL022478).
- 457 J. Pearl, “[Bayesian Analysis in Expert Systems]: Comment: Graphical Models, Causality and
458 Intervention,” *Statistical science*, vol. 8, no. 3, pp. 266–269, 1993.
- 459 N. A. Rayner, D. E. Parker, E. B. Horton, C. K. Folland, L. V. Alexander, D. P. Rowell, E. C. Kent, and
460 A. Kaplan, “Global analyses of sea surface temperature, sea ice, and night marine air temperature
461 since the late nineteenth century,” *Journal of Geophysical Research: Atmospheres*, vol. 108, no. 14,
462 p. 4407, 2003.
- 463 L. R. Rabiner, “A tutorial on hidden Markov models and selected applications in speech recognition,”
464 *Proceedings of the IEEE*, vol. 77, no. 2, pp. 257–286, Feb. 1989.
- 465 Rasmusson, E.M. and Carpenter, T.H., 1982. Variations in tropical sea surface temperature and surface
466 wind fields associated with the Southern Oscillation/El Niño. *Monthly Weather Review*, 110(5),
467 pp.354-384.
- 468 S. Stevenson, B. Fox-Kemper, M. Jochum, R. Neale, C. Deser, and G. Meehl. Will there be a significant
469 change to El Nino in the 21st century? *Journal of Climate*, 25(6):2129-2145, March 2012.

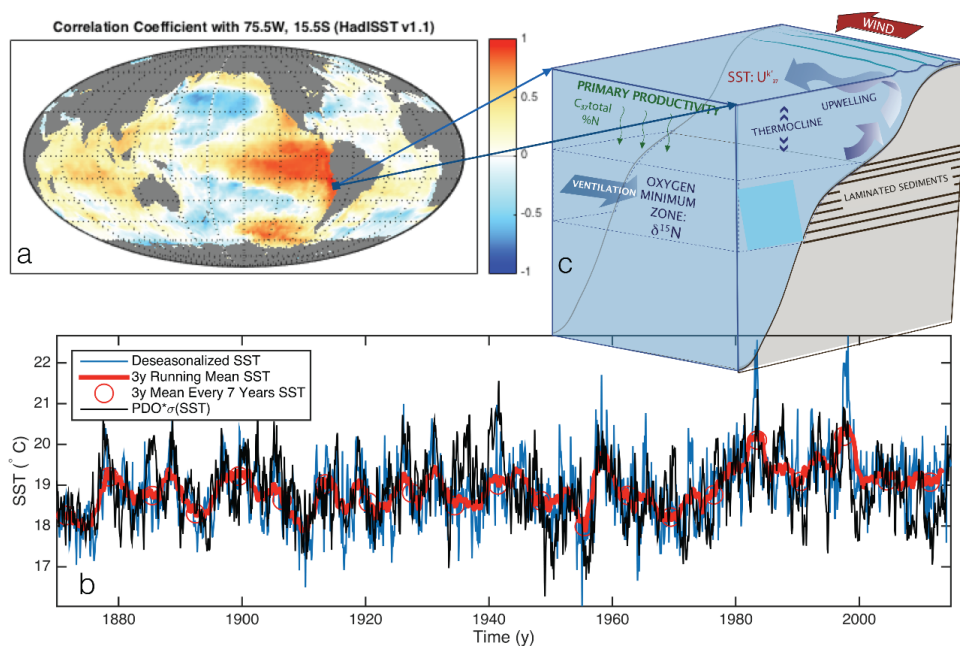


- 470 L. Stramma, G. C. Johnson, J. Sprintall, and V. Mohrholz, 2008. Expanding oxygen-minimum zones in
471 the tropical oceans. *Science*, 320(5876), pp.655-658.
- 472 P. Viefers, *Bayesian Inference for the Mixed-Frequency VAR Model*. 2011.
- 473 J. B. Weiss, 2003. *Tellus A*, 55, 208–218.
- 474 J. B. Weiss, B. Fox-Kemper, D. Mandal, A. D. Nelson, and R. K. P. Zia. Nonequilibrium oscillations,
475 probability angular momentum, and the climate system. *Dynamics and Statistics of the Climate*
476 *System*, December 2016. Submitted.
- 477 Zia, R.K.P., Weiss, J.B., Mandal, D. and Fox-Kemper, B., 2016, September. Manifest and Subtle Cyclic
478 Behavior in Nonequilibrium Steady States. In *Journal of Physics: Conference Series* (Vol. 750, No. 1,
479 p. 012003). IOP Publishing.
- 480



481 **Figures**

482



483

484

485

486

487

488

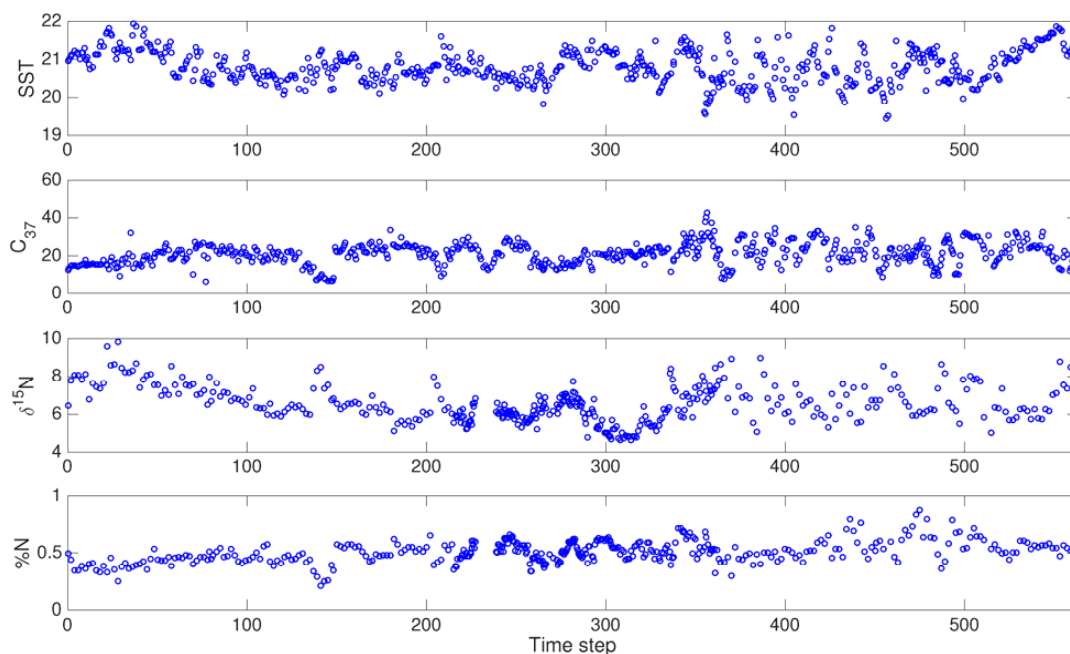
489

490

491

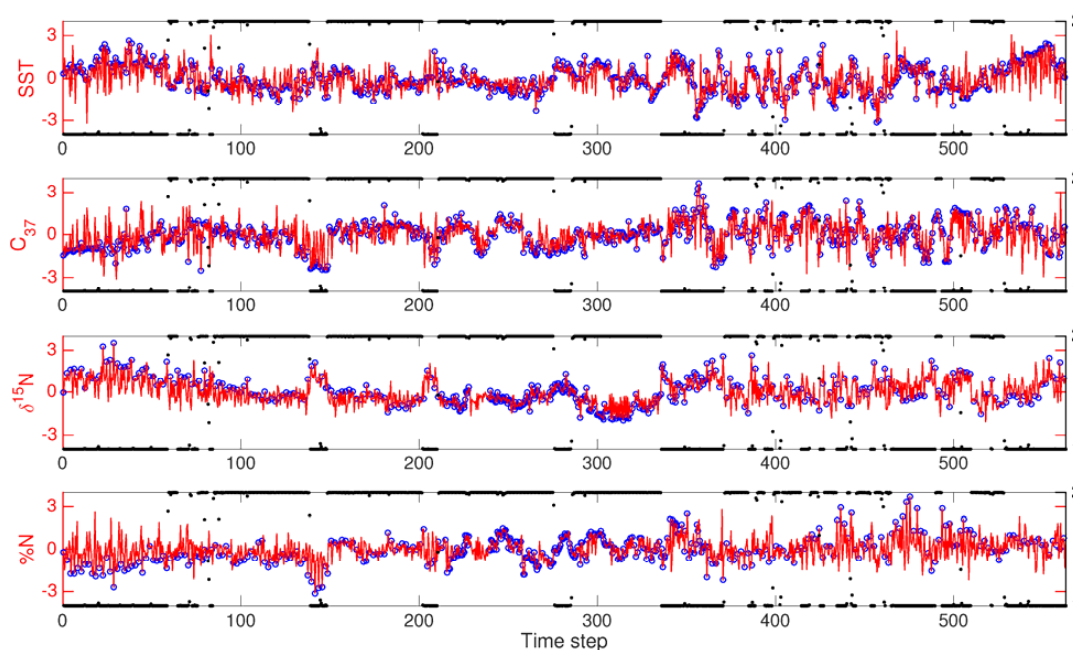
492

Figure 1 a) Location of the site MW8708-PC2 (15.1°S, 75.7°W, water depth of 250m), superimposed on the correlation of the SST gridpoint nearest that location with each SST gridpoint globally (using HadISST data, Rayner et al. 2003). b) Time series of sea surface temperature with climatological 1900-1914 seasonal cycle removed (blue), 3-year running mean of this SST (red), Pacific Decadal Oscillation principle component time series (Mantua et al. 1997, Deser et al. 2010) which has been rescaled to have the same variance as the SST (black). The red circles are exemplars of 3-year averages plotted every seventh year. c) A schematic of the region, illustrating the proxies examined (SST; C_{37} ; $\delta^{15}N$; %N) and local physical processes (wind-driven upwelling, thermocline, oxygen minimum zone).

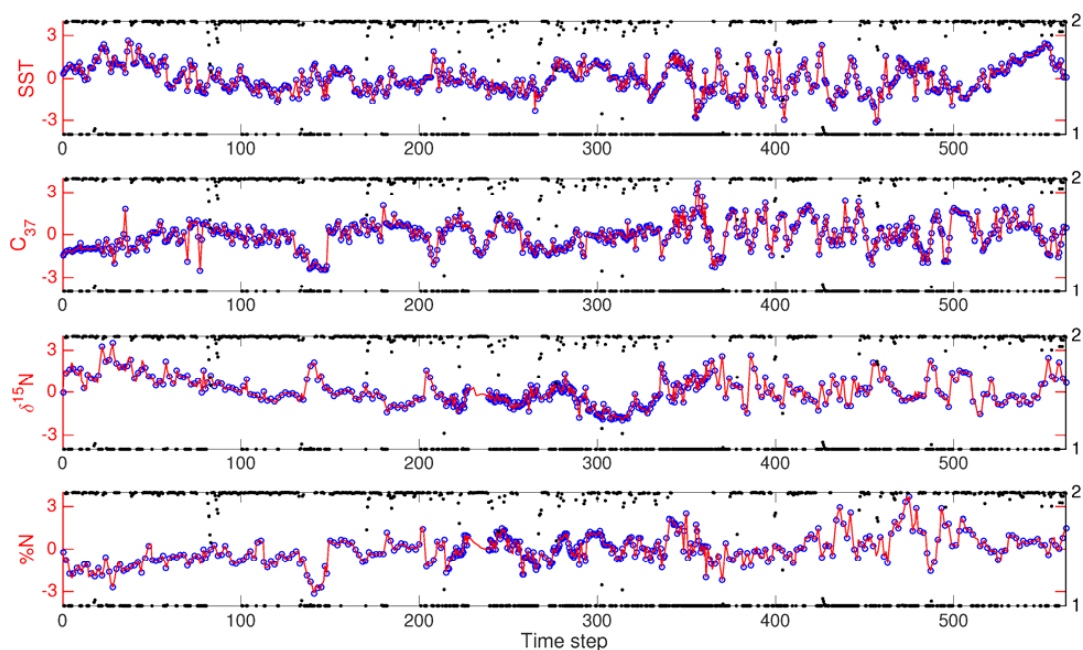


493
494
495
496

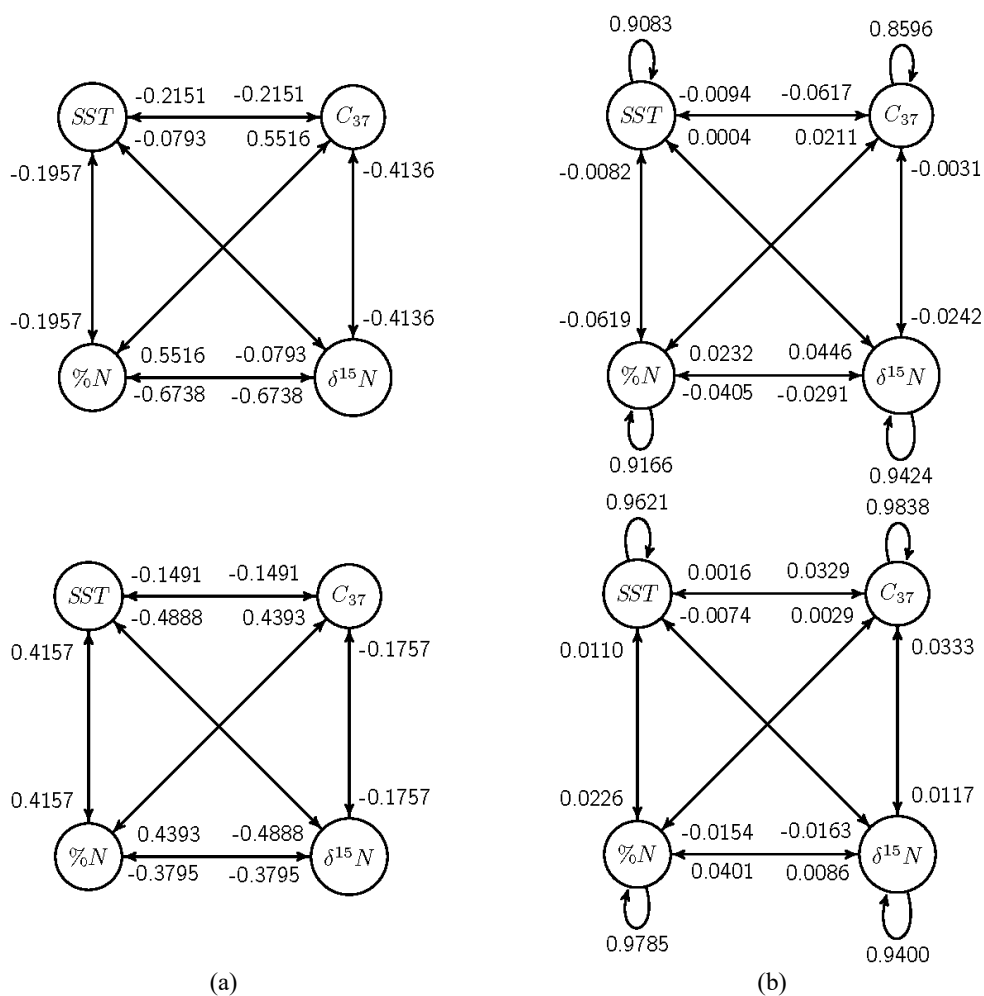
Figure 2 Observed data for time steps 0 to 563 (0.60 to 9.44 kA B.P.), with being the most recent point (time increasing to the right). 47% SST and C_{37} are missing, and 65% of $\delta^{15}N$ and %N are missing.



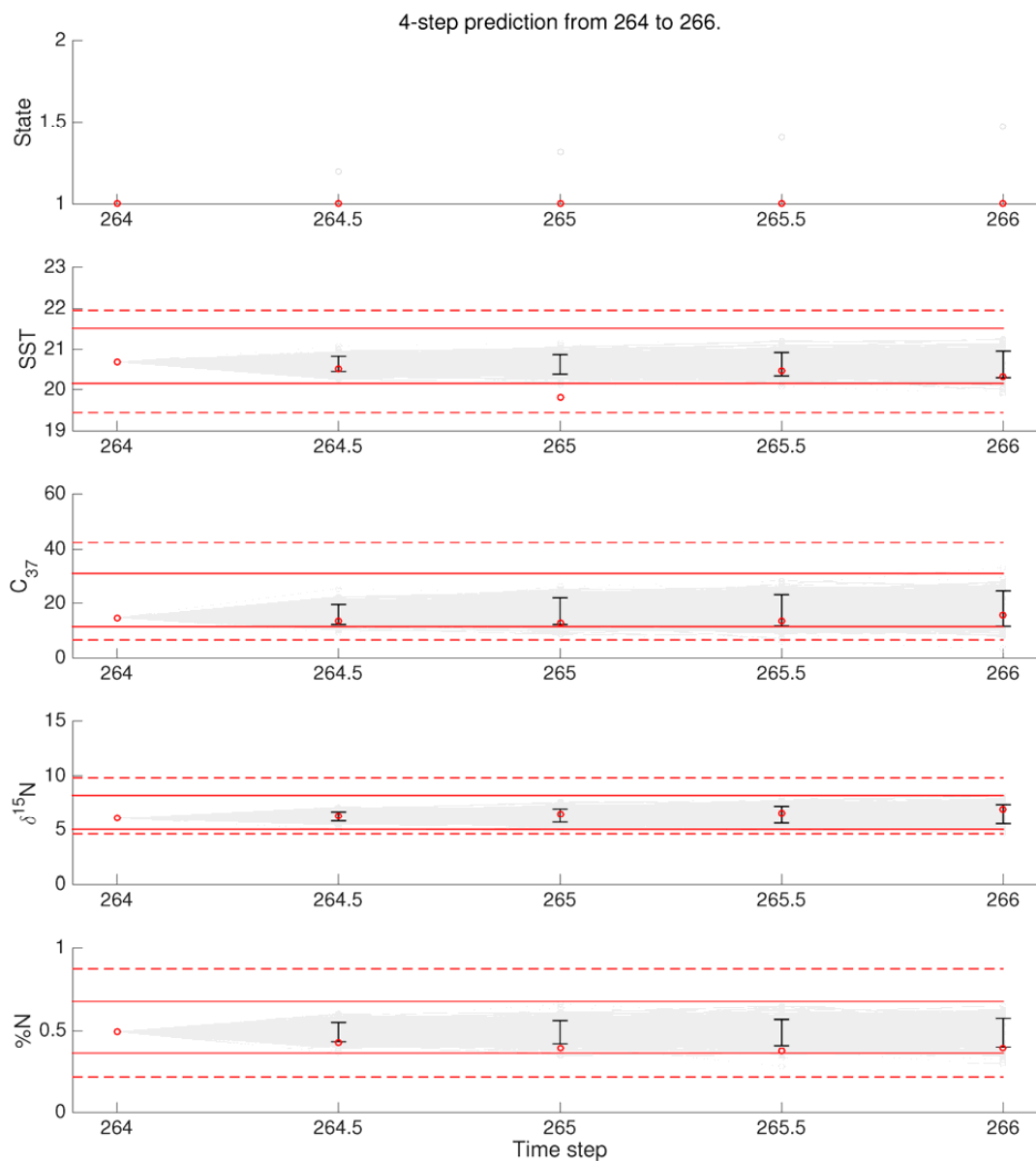
497
498 Figure 3 [HMM] State assignments by the HMM (black dots). State 1 is indicated by a black dot near the
499 lower side of each graph, indicating the probability of being in the noisy state. State 2 is indicated by a
500 black dot near the upper side of the graph. Indeterminate states are indicated by black dots in the middle
501 of the graph. Also shown are observations (blue circles) whose missing parts are imputed by expectation
502 values from the Kalman filter (red lines): SST , C_{37} , $\delta^{15}N$, and $\%N$ (from top to bottom).
503



504
505 Figure 4 [AR-HMM] State assignments by the HMM (black dots). State 1 is indicated by a black dot near
506 the lower side of each graph, indicating the probability of being in the noisy state. State 2 is indicated by a
507 black dot near the upper side of the graph. Indeterminate states are indicated by black dots in the middle
508 of the graph. Also shown are observations (blue circles) whose missing parts are imputed by expectation
509 values from the Kalman filter (red lines): SST , C_{37} , $\delta^{15}N$, and $\%N$ (from top to bottom).
510



511 Figure 5 Dependencies among observations and hidden states through a visual schematic of the
 512 correlation matrices for (a) HMM and (b) AR-HMM. Nodes are connected with an arrow if one node at
 513 the head of an arrow depends on another node at the origin of an arrow. The loopback dependencies in b)
 514 indicate a correlation of the present state of that variable with its value at a previous time.
 515



516
517 Figure 6 [AR-HMM] Results of 4-step prediction from $t=264$ to 266. The multiple grey lines indicate
518 1000 individual forecasts that differ in noise and state transitions. The black errorbars indicate the 1000-
519 forecast 0.05 quantile and 0.95 quantile, and the red circles indicate the observed values. The red dotted
520 lines indicate the range of the observation data and the solid red lines show the 0.05 quantile to 0.95
521 quantile of the observed data.

522
523



524 **Tables**

525 Table 1 [HMM] Parameters estimated for the HMM.

	State 1 (Noisy)				State 2 (Calm)					
	<i>SST</i>	<i>C</i> ₃₇	$\delta^{15}N$	% <i>N</i>	<i>SST</i>	<i>C</i> ₃₇	$\delta^{15}N$	% <i>N</i>		
<i>c</i>	[0.5044	-0.1731	0.7302	0.0602]	[-0.4007	0.1769	-0.5051	-0.0728]		
Σ	[0.9962	-0.2371	-0.0818	-0.1988	[0.5076	-0.0479	-0.2130	0.1769		
	-0.2371	1.4041	-0.3311	0.7157	-0.0479	0.5212	-0.0875	0.2075		
	-0.0818	-0.3311	0.4766	-0.4672	-0.2130	-0.0875	0.3323	-0.1307		
	-0.1988	0.7157	-0.4672	1.0716	0.1769	0.2075	-0.1307	0.3702		
Transition Probability	[0.9555				0.0445]	[0.0341				0.9659]

526

527

528 Table 2 [AR-HMM] Parameters estimated for the AR-HMM.

	State 1 (Noisy)				State 2 (Calm)					
	<i>SST</i>	<i>C</i> ₃₇	$\delta^{15}N$	% <i>N</i>	<i>SST</i>	<i>C</i> ₃₇	$\delta^{15}N$	% <i>N</i>		
<i>c</i>	[0.0211	-0.0001	0.0557	-0.0067]	[-0.0185	-0.0012	-0.0358	0.0124]		
θ	[0.9083	-0.0094	0.0004	-0.0082	[0.9621	0.0016	-0.0074	0.0110		
	-0.0617	0.8596	-0.0031	0.0211	0.0329	0.9838	0.0333	0.0029		
	0.0446	-0.0242	0.9424	-0.0291	-0.0163	0.0117	0.9400	0.0086		
	-0.0619	0.0232	-0.0405	0.9166	0.0226	-0.0154	0.0401	0.9785		
Σ	[0.2157	-0.0250	-0.0080	0.0361	[0.0333	-0.0037	0.0105	-0.0012		
	-0.0250	0.2430	-0.0692	0.0616	-0.0037	0.0334	0.0022	0.0053		
	-0.0080	-0.0692	0.1644	-0.0397	0.0105	0.0022	0.0063	-0.0013		
	0.0361	0.0616	-0.0397	0.2066	-0.0012	0.0053	-0.0013	0.0063		
Transition Probability	[0.8077				0.1923]	[0.1720				0.8280]

529

530

531 Table 3 [HMM] Correlation matrix of *SST*, *C*₃₇, $\delta^{15}N$, and %*N* for each HMM state. The correlation
 532 matrices are obtained directly from the data set augmented by their expected values once the state at each
 533 time is known.

	State 1 (Noisy)				State 2 (Calm)			
	[1.0000	-0.2151	-0.0793	-0.1957	[1.0000	-0.1491	-0.4888	0.4157
	-0.2151	1.0000	-0.4136	0.5516	-0.1491	1.0000	-0.1757	0.4393
	-0.0793	-0.4136	1.0000	-0.6738	-0.4888	-0.1757	1.0000	-0.3795
	-0.1957	0.5516	-0.6738	1.0000	0.4157	0.4393	-0.3795	1.0000

534

535



536

537 Table 4 [AR-HMM] Correlation matrix of SST , C_{37} , $\delta^{15}N$, and $\%N$ for each AR-HMM state. The
 538 correlation matrices are obtained directly from the data set augmented by the Kalman filter imputed
 539 values once the state at each time is known.

	State 1 (Noisy)		State 2 (Calm)
$\begin{bmatrix} 1.0000 & -0.2139 & 0.1081 & -0.0145 \\ -0.2139 & 1.0000 & -0.3406 & 0.4048 \\ 0.1081 & -0.3406 & 1.0000 & -0.4365 \\ -0.0145 & 0.4048 & -0.4365 & 1.0000 \end{bmatrix}$		$\begin{bmatrix} 1.0000 & -0.2555 & 0.2065 & -0.0175 \\ -0.2555 & 1.0000 & -0.2853 & 0.3684 \\ 0.2065 & -0.2853 & 1.0000 & -0.3714 \\ -0.0175 & 0.3684 & -0.3714 & 1.0000 \end{bmatrix}$	

540

541

542 Table 5 [AR-HMM] Squared bias, variance, and MSE of the prediction up to 266. (The numbers in
 543 parenthesis represent the percentage over the longest prediction.)

Length of Prediction		1	2	4	30
SST	Bias ²	0.0305	0.1005	0.0919	0.1004
	Variance	0.0237	0.0540	0.0404	0.1386
	MSE	0.0541 (22.66)	0.1545 (64.64)	0.1323 (55.34)	0.2390 (100)
C_{37}	Bias ²	2.0373	2.6533	3.2239	68.0915
	Variance	4.9198	9.6830	15.2824	26.5790
	MSE	6.9571 (7.35)	12.3363 (13.03)	18.5064 (19.55)	94.6705 (100)
$\delta^{15}N$	Bias ²	0.0691	0.1700	0.3130	0.4763
	Variance	0.0849	0.1996	0.3026	0.5750
	MSE	0.1540 (14.65)	0.3695 (35.15)	0.6155 (58.55)	1.0513 (100)
$\%N$	Bias ²	0.0002	0.0003	0.0083	0.0154
	Variance	0.0011	0.0018	0.0027	0.0053
	MSE	0.0012 (5.97)	0.0021 (10.20)	0.0110 (53.41)	0.0207 (100)

544